Design strategy and comparison of four PM motor topologies for a 2 kW traction application (repository copy)

Article:

Pastellides, S., Gerber, S., Wang, R-J. (2019), Design and comparison of four PM motor topologies for a 2 kW traction application, *Proc. the 27th Southern African Universities Power Engineering Conference*, (SAUPEC), pp. 358-363, 28-30 Jan. 2019, Central University of Technology, Bloemfontein.

ISBN: 978-1-7281-0368-6 / IEEE Catalogue Number: CFP1948U-USB
http://doi.org/10.1109/RoboMech.2019.8704829

2019 SAUPEC/RobMech/PRASA Conference
Bloemfontein, South Africa, January 28-30, 2019

Design Strategy and Comparison of Four PM Motor Topologies for a 2 kW Traction Application

Stavros Pastellides, Stiaan Gerber* and Rong-Jie Wang†
Department of Electrical and Electronic Engineering
Stellenbosch University
Stellenbosch, 7600
South Africa
Email: sgerber@sun.ac.za*, rwang@sun.ac.za†

***Abstract*—This paper discusses the design optimization and comparison of four permanent magnet machines with different rotor topologies for a 2 kW traction application. The rotor topologies considered include the surface mount, spoke type, radial bar and v-shaped topologies. Special attention is given to the optimization strategy and three alternative ways of formulating the optimization problem are given and the relative merits of each formulation are discussed. Performance calculations are based on 2D finite element analyses of all the critical operating points across the required operational speed range. The objective of the optimization is to minimize the material cost of the machine. Despite the popularity of interior permanent magnet machines, this study shows that the surface mount topology can be a strong competitor in this regard, even when a constant power speed range equal to four times the base speed is required.**

***Index Terms*—Design optimization, finite element analysis, permanent magnet machines, rotating machines, traction motors**

I. Introduction

Globally, the transportation sector is still one of the largest energy consumers, where fossil fuels are the main energy sources. To develop more sustainable transportation systems, electrified power-trains are increasingly used in many countries. Comparing with internal combustion engines (ICEs), electric motors are more energy efficient and their torque-speed characteristics are better suited for traction requirements. Nowadays, almost all major automotive manufacturers are rushing to make electric vehicles (EVs). Historically, induction machines have been widely used for traction applications. In the past decade, permanent magnet (PM) machines have attracted more interest for EV applications [1]–[4].

Different PM machine topologies have been proposed, which can be classified into two categories, namely, surface-mounted and interior PM machines. Surface-mounted PM machines (SPM) offer the advantage of simplicity of manufacturing. However, glass fiber bandage is usually required to ensure mechanical integrity of the rotor at high speeds. In contrast, the interior PM machines (IPM) are generally less prone to such problems. The IPMs also boast an advantage by having a larger d-axis and q-axis inductance difference (also called *magnetic saliency*). This contributes to a higher reluctance torque, which in turn delivers a larger overall torque in the high speed field-weakening range [5].

In this paper, a comparative study of a SPM machine and three different IPM machines are conducted for EV applications. The selected candidate machines are individually designed and optimized using a 2D in-house finite-element method (FEM) package. The primary objective of the optimization was to minimize the cost for each design while maintaining a specified constant torque and constant power region for traction applications. By minimizing the cost for each design and ensuring a 2 kW nominal power output, a comparison can be made of the most cost effective designs.

The rest of the paper is structured as follows: Section II discusses the selected machine topologies and specifications for each design, to ensure a fair comparison. Section III describes the optimization design strategy. Section IV discusses and compares the different designs in terms of dimensions, mass, volume, demagnetization, currents and cost. Relevant conclusions are drawn in Section V.

II. Machine Topologies and Design Specifications

A. Selected Topologies

As shown in Fig. 1, the rotor topologies of the selected three IPM designs are spoke-type PM (STPM), radial-bar PM (RBPM) and V-shaped PM (VPM) types. The STPM is seen to yield a higher air-gap flux density due to flux concentration effects. Owing to its high magnetic loading, a higher efficiency can be found with a smaller electric loading for the same power output, however at the cost of a larger PM usage [6]. For the RBPM topology, the PMs are situated closer to the rotors surface requiring a smaller PM volume. This topology also features a higher flux weakening capability [4], [7], [8]. The VPM structure lies between the STPM and RVPM designs. It allows for the flexibility of adjusting the V-angle, which causes the flux concentration to change, which in turn affects the saliency ratio of the d-q inductances. This angle can be optimized in order to achieve the desired results. This topology boasts good performance in both torque and extended speed operation [4], [5]. Lastly, the SPM makes the most effective use of the PM material as the design reduces the amount of leakage flux, which occurs through the rotor. Generally, this configuration is not suited for high speed application. The reluctance variation between the direct and quadrature axis is much smaller compared to the other machines, which may have consequences during control and operation [6].

978-1-7281-0369-3/19/$31.00 ©2019 IEEE

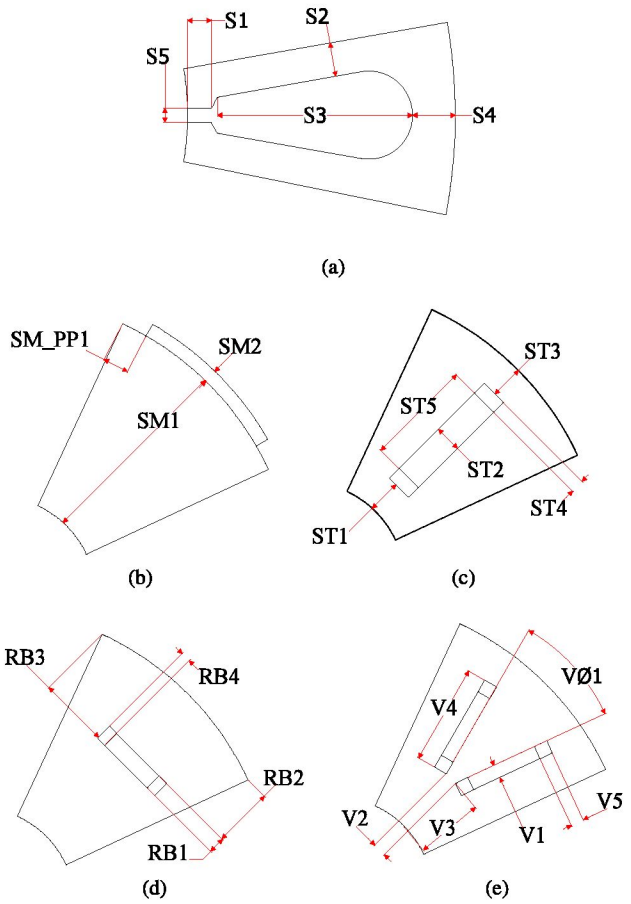

Fig. 1. Configurations of various topologies with dimension variables a) Stator slot b) Surface mount PM design c) Spoke type design d) Radial bar design e) V-shape design

B. Design Specifications

The design specifications are summarized in Table I. For each topology, candidate designs with 4-, 6- and 8-pole are all analyzed. The stator design for all the design studies is confined to a 3-phase, 36-slot, double-layer distributed winding. In order to characterize both the constant torque speed range (CTSR) and constant power speed range (CPSR), three design points are used as seen in Fig. 2. These design points are critical performance assessment points for traction application, as they specify the capabilities of the machine.

In Table I, the minimum torque is set at 15.3 Nm for Point 0 and Point 1 and 3.8 Nm for Point 2. By creating these constraints, it ensures a constant torque and constant power range will be kept for each design. For this study, a CPSR of 4 is defined as part of the design specifications, which is a typical value for traction application [5].

The inverter requirements are set by keeping the voltage V_{LL} and armature current I_S at nominal values of 48 V and 27 A, respectively. These values are typical for battery operated EV's. The apparent power of the inverter is set as

$$S = \sqrt{3} V_{LL} I_S \quad \text{(VA)} \tag{1}$$

Also by specifying the winding temperature to be 120°C, and constraining the maximum losses to be an overestimate of 200 W, the thermal loading and efficiency are inherently constrained. To mitigate the demagnetization risks (especially

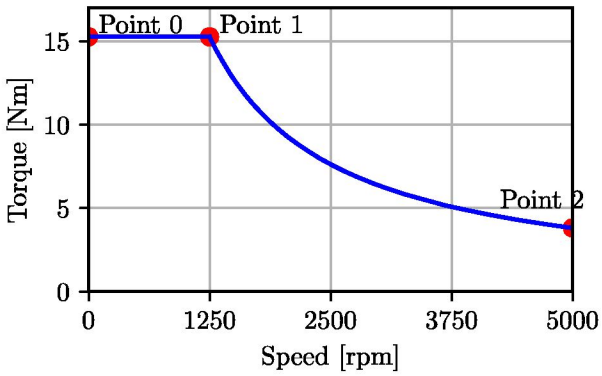

Fig. 2. Torque-speed curve specification.

TABLE I
SPECIFICATIONS FOR 2 KW TRACTION MOTOR DESIGNS

Parameters	Value
Phases	3
Slots	36
Air gap length (mm)	1
Remnant flux density (T)	1.39
Recoil permeability	1.05
Fill Factor	40%
Shaft size (Diameter) (mm)	30
Nominal power (kW)	2
Nominal voltage (V_{LL}) (V)	48
Nominal current (I_S) (A)	27
Peak loss (W)	200
Winding temperature (°C)	120
Initial speed (Point 0) (rpm)	1
Base speed (Point 1) (rpm)	1250
Max speed (Point 2) (rpm)	5000
Minimum Point 1 torque (Nm)	15.3
Minimum Point 2 torque (Nm)	3.8
Demagnetization value (T)	0.2
Demagnetization margin (T)	0.01
PM type	NdFeB N48H

under flux weakening operation), a constraint is also kept for a demagnetization margin, which is set so that the flux density of the PMs must stay above the "knee" point, as seen in Fig. 3 and Table I.

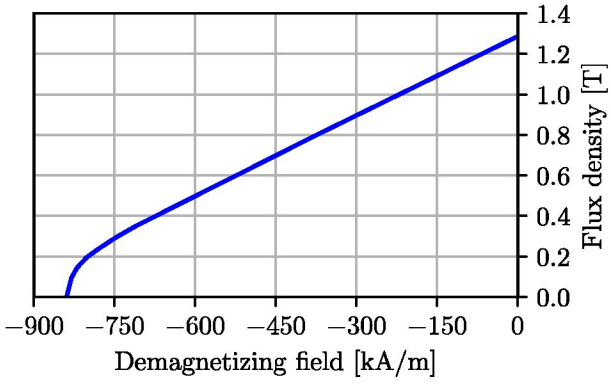

Fig. 3. Demagnetization curve

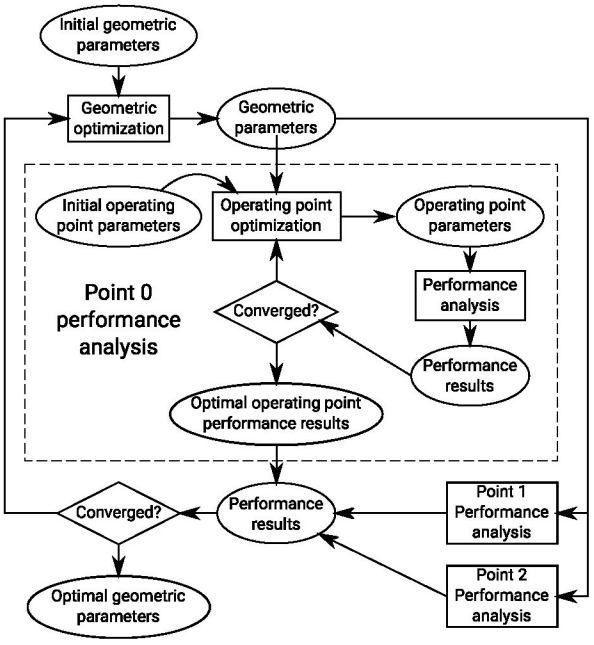

(a)

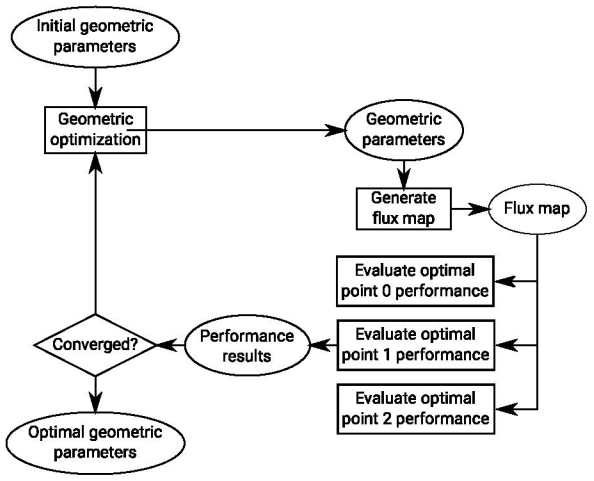

(b)

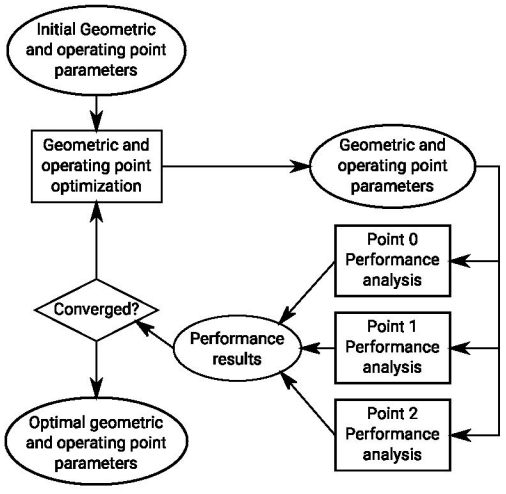

(c)

Fig. 4. Different optimization strategies for traction machine design. a) Solving optimal operating points at each step. b) Finding operating points from flux map. c) Optimizing operating points along side geometric parameters.

III. Optimization Strategy

Optimizing electrical machine designs for traction applications is more challenging than optimizing designs for fixed speed applications or variable speed applications where flux weakening operation is not required. This is because in traction applications, different performance characteristics are required over the machine's operational speed range. Here, we consider optimization strategies based on finite element analyses (FEA) of machine performance.

To be able to compare the different designs accurately and fairly, multiple geometric parameters are adjusted for both the rotor and stator. These variables are illustrated in Fig. 1. By adjusting both parts of the machine, the results are seen to be fair and unbiased. The variables that were adjusted for the stator and each topology are shown in Fig. 1. The optimization process was performed with a 2D rotating analysis.

Although methods exist which perform a finite element analysis on a single operating point, typically point 1 in Fig. 2, and then estimates the performance in other points based on simplified analytical approximations, we focus on optimization strategies where all critical points are analyzed using FEA. This provides greater accuracy. Design point 0 and point 1 ensures the torque developed by the machine is above a certain threshold. This ensures a CTSR for the machine for each design. At point 0, the torque may be higher than at point 1, such as for heavy traction application. To ensure a CPSR, points 1 and 2 are used. At both these design points, the power of the machine must be kept at nominal power as stated in section II.

Three different finite element based optimization strategies are illustrated in Fig. 4. The first is a nested optimization approach, shown in Fig. 4a. The geometric variables are optimized in the outer loop. For each of the operating points analyzed in the outer loop, an inner optimization process finds the optimal (maximum torque per ampere) dq-currents. Some of the design constraints are handled in the inner loop, e.g. the voltage limits. For this strategy, the outer optimization problem may be formulated as:

$$\begin{aligned} \text{Minimise:} \quad & F(\mathbf{X_g}) = C_{\text{total}} && (2)\\ \text{Subject to:} \quad & I_{\phi 1} \leq 27\,\text{A} && (3)\\ & P_{\text{loss1}} \leq 200\,\text{W} && (4)\\ & B_{MM1} \geq 0.01\,\text{T} && (5)\\ & P_{\text{loss2}} \leq 200\,\text{W} && (6)\\ & B_{MM2} \geq 0.01\,\text{T} && (7) \end{aligned}$$

where $\mathbf{X_g}$ represents the vector of geometric design variables, C_{total} is the total material cost of the machine, P_{loss} is the total losses at the specified operating point and B_{MM} is the demagnetization margin at the specified operating point. The inner optimization loop for point 1, for example, may be formulated as:

$$\begin{aligned} \text{Minimise:} \quad & F(\mathbf{X_{i1}}) = I_{\phi 1} && (8)\\ \text{Subject to:} \quad & T_1 \geq 15.3\,\text{Nm} && (9)\\ & V_{LL1} \leq 48\,\text{V} && (10) \end{aligned}$$

where $\mathbf{X_i}$ represents the dq-currents, I_ϕ is the RMS phase current, T is the output torque and V_{LL} is the RMS line-to-line voltage, all referring to point 1 in this case.

The second approach, shown in Fig. 4b is similar to the first, except that flux maps are used to find the optimal operating points instead of inner optimization loops. For each set of geometric parameters, mappings of the dq-fluxes versus dq-currents are generated using FEA. Using the flux maps, the optimal dq-currents for each operating point can be found very efficiently and the machine's performance can be evaluated. However, the computational cost of generating a flux map is relatively high.

Upon closer inspection, it can be seen that in the first two approaches some scenarios may arise, which have to be dealt with in a special way. For example, what should be done if (9) can not be satisfied within the search space defined by the bounds on the design variables and the inner optimization process fails? Although there are ways to deal with such situations, additional complexity is introduced and, perhaps more importantly, these special cases can have a negative impact on the performance of the outer optimization loop.

A third approach, shown in Fig. 4c, consists of a single optimization process where the geometric parameters and the dq-currents at each operating point form the set of design variables to be optimized. Using this approach, a larger number of design variables need to be optimized in the (single) outer loop and during the optimization process, each geometry is not necessarily evaluated at its optimal operating points. However, this strategy has significant advantages in terms of the numerical conditioning of the optimization problem, which is vitally important when computationally efficient gradient-based optimization algorithms are employed. In this case, the optimization problem is formulated as:

$$\begin{aligned}
\text{Minimise:} \quad & F(\mathbf{X}) = C_{\text{total}} && (11)\\
\text{Subject to:} \quad & T_1 \geq 15.3\,\text{Nm} && (12)\\
& V_{LL1} \leq 48\,\text{V} && (13)\\
& I_{\phi 1} \leq 27\,\text{A} && (14)\\
& P_{\text{loss1}} \leq 200\,\text{W} && (15)\\
& B_{MM1} \geq 0.01\,\text{T} && (16)\\
& T_2 \geq 3.8\,\text{Nm} && (17)\\
& V_{LL2} \leq 48\,\text{V} && (18)\\
& I_{\phi 2} \leq 27\,\text{A} && (19)\\
& P_{\text{loss2}} \leq 200\,\text{W} && (20)\\
& B_{MM2} \geq 0.01\,\text{T} && (21)
\end{aligned}$$

where $\mathbf{X}$ represents the vector of design variables, including the geometric variables, the dq-currents at each operating point and the number of coil turns, which is treated as a floating point value. Importantly, in this case all the objective and constraints are smooth functions of the design variables.

Based on this discussion and some practical evaluation, the third approach was selected as the most appropriate for traction design optimization and employed in this study. As an additional measure to ensure that a good optimal solution was found, each optimization process was conducted from multiple sets of initial values for the design variables.

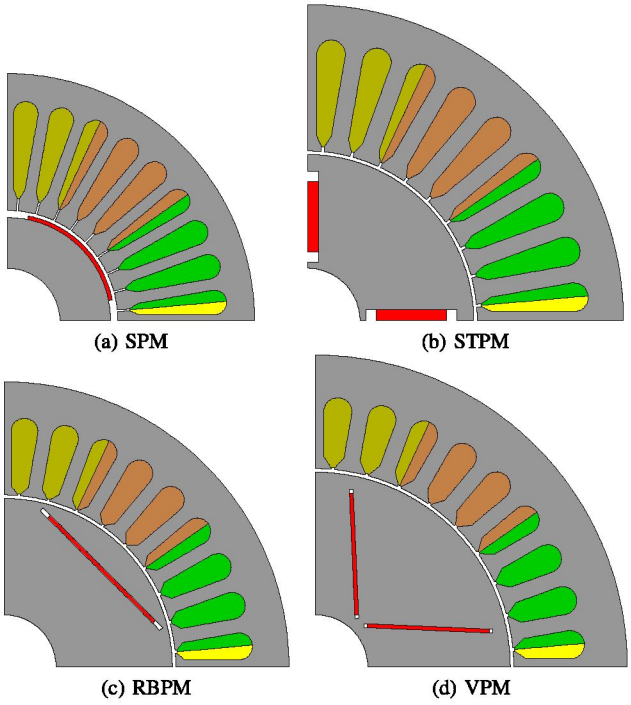

Fig. 5. Four pole configuration

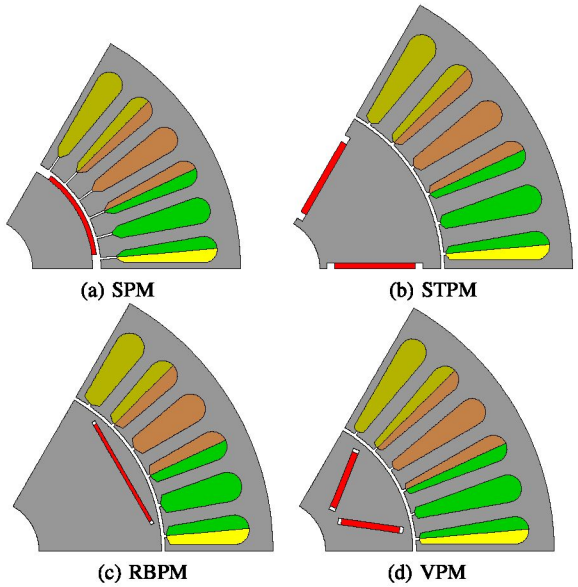

Fig. 6. Six pole configuration

IV. Comparison of Designs

Figs. 5 - 7 show the optimal designs for the different rotor topologies and pole pair configurations. All parameters for each design is shown in Table II, from the stator parameters to the coil turns. The geometric parameters listed in Table II are defined in Fig. 1. The coil turns shown are calculated by the optimisation algorithm. These would need to be rounded to integer values for manufacturing purposes. The total cost, and material masses for the designs are listed in Table III. From Table III, it is clear that the SPM topologies performed best, achieving the lowest cost in 4-, 6-, and 8- pole configurations. As the cost of the machines are directly proportional to their mass, the cost is largely dependent on the PM mass. This is

TABLE II
OPTIMUM PARAMETERS FOR EACH TOPOLOGY

	SPM			STPM			RBPM			VPM		
Parameter	**4–pole**	**6–pole**	**8–pole**	**4–pole**	**6–pole**	**8–pole**	**4–pole**	**6–pole**	**8–pole**	**4–pole**	**6–pole**	**8–pole**
Outer radius	71	74.8	79.9	90.8	87.63	92.37	81.9	82.26	86.15	94.32	78.16	83.8
Stack length	138	89.7	71.8	128.9	104.3	71.47	105.6	86.5	71	89.62	115.8	58.9
Total volume	2.19 L	1.58 L	1.44 L	3.34 L	2.52 L	1.92 L	2.23 L	1.84 L	1.66 L	2.51 L	2.22 L	1.3 L
S1	3.5	4.7	3.6	0.5	2.3	0.5	0.5	0.6	0.5	0.5	1.1	1
S2	1.7	1.9	2	2.7	2.6	3	2.1	2	2.2	2.4	2.2	2.3
S3	28	29	26	36	26	31	22	24	27	20	32	28
S4	7.8	6.5	5.5	9.2	7	6	10	6.5	5.6	12	7	6
S5	0.3	0.3	0.4	0.7	0.6	0.6	0.4	0.5	0.5	0.5	0.4	0.4
SM1	20.85	24.07	34									
SM2	1.07	1.35	1									
SM_PP1	5.78	4.08	4.32									
ST1				3.89	2	2.6						
ST2				4.08	2.38	1.73						
ST3				3.13	4.92	2.4						
ST4				1	2.65	2.51						
ST5				26.5	33.2	34.9						
RB1							1.14	1	1.09			
RB2							1	1.19	1			
RB3							1	1	1			
RB4							2.92	1	1			
V1										1.11	1.81	1
V2										1.06	1.07	1.04
V3										3.62	6.01	4.7
V4										37.08	18.87	27.03
V5										1	1	1
Vθ1										47.5°	38.1°	24.35°
Coil turns	3.82	5.02	5.44	3.7	4.33	4.8	3.89	4.99	5.65	3.88	5.36	5.88

* All geometric parameters in mm, unless indicated otherwise

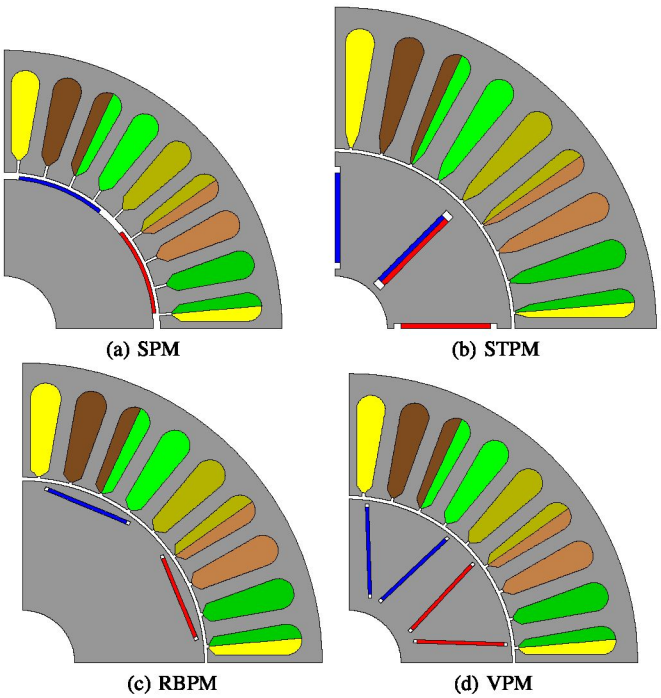

Fig. 7. Eight pole configuration

due to the cost per kilogram of PMs being much larger than silicon steel and copper, as seen in Table IV [9].

All topologies performed better as the pole count was increased from 4 to 8. This indicates that the benefits of having a higher pole count, i.e. higher torque production outweighs the disadvantages associated with higher operating frequencies for the specifications considered in this study.

The SPM topologies have an interesting stator design compared to the other topologies. In each case, a long, thin slot opening gap resulted from the optimization. This increases the leakage paths of the slot, which in turn allows for a wide field weakening range.

For the 8- pole configuration, the VPM topology's performance nearly matched that of the SPM topology. This confirms that the VPM topology is an attractive candidate, since other considerations such as rotor integrity at high speed and low risk of demagnetization may make this topology the preferred choice for practical purposes. As seen in Table V, the SPM lies close to the demagnetization region. This may lead to a slight concern if the magnets were subjected to a larger demagnetizing field such as may occur due to a short circuit from the inverter. Generally, the IPM designs are further above this region, showing that even with a larger demagnetizing field, no permanent demagnetization will occur. Future work may include more detailed analyses of the demagnetization risk under short-circuit conditions, as part of the optimization process.

Table VI shows the d- and q- axis currents for points 1 and 2, as calculated from the optimization process. The fact that the currents produced by the optimization process resulted

TABLE III
COMPARED COSTS AND MASS FOR EACH DESIGN

Parameter	SPM	STPM	RBPM	VPM
4–pole				
Total Cost	57.76 $	96.32 $	58 $	62.1 $
Total Mass	14.8 kg	23.76 kg	16.27 kg	17.3 kg
Steel Mass	10.1 kg	17.15 kg	12.24 kg	13.36 kg
Copper Mass	4.37 kg	6.2 kg	3.87 kg	3.72 kg
PM Mass	0.16 kg	0.41 kg	0.15 kg	0.21 kg
6–pole				
Total Cost	44.08 $	68.35 $	48.4 $	51.94 $
Total Mass	10.8 kg	17.05 kg	13.05 kg	11.92 kg
Steel Mass	7.33 kg	12.82 kg	9.43 kg	7.98 kg
Copper Mass	3.32 kg	3.89 kg	3.49 kg	3.71 kg
PM Mass	0.15 kg	0.34 kg	0.13 kg	0.23 kg
8–pole				
Total Cost	38.9 $	58.87 $	44.95 $	40.94 $
Total Mass	10.09 kg	14.58 kg	11.89 kg	9.46 kg
Steel Mass	7.12 kg	10.82	8.41 kg	6.4 kg
Copper Mass	2.86 kg	3.48	3.37 kg	2.88 kg
PM Mass	0.11 kg	0.28	0.11 kg	0.18 kg

TABLE IV
COSTS OF MATERIALS

Material	Cost
PM	$50/kg
Silicon steel	$2/kg
Copper	$6.67/kg

in designs in which most of the constraints are active, or in other words, only closely satisfied, validates the effectiveness of the optimization process.

V. CONCLUSION

A comparative analysis was conducted between four different PM design topologies, namely the SPM, STPM, RBPM and VPM. Each topology is designed through a optimization design method, which uses operating points along side geometric parameters. Each topology has been optimized with different pole pairs and compared. The costs for each design was minimised while keeping the CTSR and CPSR the same for each design. It was found that the SPM was the most cost effective for the given specifications, but

TABLE V
DEMAGNETIZATION MARGIN FOR EACH DESIGN

Operating point	SPM	STPM	RBPM	VPM
4–pole				
Point 0	0.056 T	0.837 T	0.2 T	0.288 t
Point 1	0.01 T	0.834 T	0.163 T	0.288 T
Point 2	0.021 T	0.841 T	0.131 T	0.321 T
6–pole				
Point 0	0.214 T	0.781 T	0.361 T	0.56 T
Point 1	0.189 t	0.746 t	0.309 T	0.492 T
Point 2	0.22 T	0.736 T	0.27 T	0.473 T
8–pole				
Point 0	0.12 T	0.644 T	0.318 T	0.271 T
Point 1	0.08 T	0.615 T	0.286 T	0.24 T
Point 2	0.095 T	0.58 T	0.235 T	0.194 T

TABLE VI
DQ CURRENTS AT DESIGN POINTS

Parameter	SPM	STPM	RBPM	VPM
4–pole				
Point 1 D-current	-2.19 A	-2.97 A	-4.19 A	-3.9 A
Point 1 Q-current	4.91 A	2.71 A	4.01 A	4.5 A
Point 2 D-current	-5.18 A	-3.72 A	-5.36 A	-5.6 A
Point 2 Q-current	1.19 A	0.64 A	0.88 A	0.97 A
6–pole				
Point 1 D-current	-2.87 A	-3.1 A	-4.31 A	-3.79 A
Point 1 Q-current	5.55 A	3.72 A	4.28 A	4.42 A
Point 2 D-current	-5.86 A	-4.55 A	-5.59 A	-5.51 A
Point 2 Q-current	1.35 A	0.82 A	0.95 A	0.99 A
8–pole				
Point 1 D-current	-2.8 A	-2.82 A	-4 A	-3.8 A
Point 1 Q-current	5.99 A	4.37 A	4.52 A	5.54 A
Point 2 D-current	-6.32 A	-4.91 A	-5.69 A	-6.41 A
Point 2 Q-current	1.45 A	1.03 A	1.01 A	1.25 A

may be at risk of demagnetization if a greater external field is applied to the magnets. The VPM showed improved results compared to the other two IPM topologies, for the eight pole design, and the cost effectiveness is close to the SPM. This shows that the VPM may show improved results in further studies if flux barriers are used.

REFERENCES

[1] J. de Santiago, H. Bernhoff, B. Ekergård, S. Eriksson, S. Ferhatovic, R. Waters, and M. Leijon, "Electrical motor drivelines in commercial all-electric vehicles: A review," *IEEE Transactions on Vehicular Technology*, vol. 61, no. 2, pp. 475–484, Feb 2012.

[2] A. M. Bazzi, "Electric machines and energy storage technologies in evs and hevs for over a century," in *2013 International Electric Machines Drives Conference*, May 2013, pp. 212–219.

[3] Y. Yang, S. M. Castano, R. Yang, M. Kasprzak, B. Bilgin, A. Sathyan, H. Dadkhah, and A. Emadi, "Design and comparison of interior permanent magnet motor topologies for traction applications," *IEEE Transactions on Transportation Electrification*, vol. 3, no. 1, pp. 86–97, March 2017.

[4] F. Ma, H. Yin, L. Wei, G. Tian, and H. Gao, "Design and optimization of IPM motor considering flux weakening capability and vibration for electric vehicle applications," *Sustainability*, vol. 10, pp. 1–15, May 2018.

[5] K. T. Chau, *Electric vehicle machines and drives*. Wiley, 2015, ch. 1-4.

[6] R. Krishnan, *Permanent Magnet Synchronous and Brushless DC Motor Drives*. CRC Press, 2010, ch. 1.

[7] L. Jolly, M. A. Jabbar, and L. Qinghua, "Optimization of the constant power speed range of a saturated permanent-magnet synchronous motor," *IEEE Transactions on Industry Applications*, vol. 42, no. 4, pp. 1024–1030, July 2006.

[8] R. Dutta and M. F. Rahman, "Design and analysis of an interior permanent magnet (IPM) machine with very wide constant power operation range," *IEEE Transactions on Energy Conversion*, vol. 23, no. 1, pp. 25–33, March 2008.

[9] P. M. Tlali, R. Wang, and S. Gerber, "Comparison of PM Vernier and Conventional Synchronous 15 kW Wind Generators," in *2018 XIII International Conference on Electrical Machines (ICEM)*, Sep. 2018, pp. 2065–2071.